



Research Article

Ultra-high resistance to electrochemical and high-temperature steam corrosion of MAO/Cr bilayer coatings fabricated on Zr alloys

Zheng Wang^{a,c,1}, Yingpeng Zhang^{b,1}, Zhichao Han^a, Zhenyu Wang^a, Wei Yang^d, Ming Li^{a,c}, Aiyang Wang^a, Peiling Ke^{a,c,*}

^a Key Laboratory of Advanced Marine Materials, Ningbo Institute of Materials Technology and Engineering, Chinese Academy of Sciences, Ningbo 315201, China

^b School of Materials and Chemical Engineering, Ningbo University of Technology, Ningbo 315211, China

^c Analytical Center, Ningbo Institute of Materials Technology and Engineering, Chinese Academy of Sciences, Ningbo 315201, China

^d School of Materials Science and Chemical Engineering, Xi'an Technological University, Xi'an 710021, China



ARTICLE INFO

Article history:

Received 19 November 2024

Revised 13 March 2025

Accepted 18 April 2025

Available online 4 June 2025

Keywords:

MAO/Cr bilayer coating

Zr alloy

HiPIMS

Electrochemical corrosion

High-temperature steam oxidation

ABSTRACT

In this work, MAO/Cr bilayer coatings were deposited on Zr alloys by combining micro-arc oxidation (MAO) and high-impulse-power magnetron sputtering (HiPIMS) techniques. The coating exhibited outstanding resistance to electrochemical and high-temperature steam corrosion. As the surface defects of the MAO interlayer increased the nucleation sites of Cr grains, it refined the grain size of the Cr top layer, which could promote the growth of passive film in lithium borate aqueous solution and enhance its corrosion resistance. Moreover, under the simulated loss-of-coolant accident (LOCA) scenario, the MAO/Cr bilayer coating exhibited a weight gain roughly 34.9 % lower than the Cr coating after oxidation for 90 min. This was primarily due to the MAO interlayer inhibiting interdiffusion at the coating-substrate interface and reducing the rapid diffusion paths for oxygen in the residual Cr coating during oxidation.

© 2025 Published by Elsevier Ltd on behalf of The editorial office of Journal of Materials Science & Technology.

1. Introduction

Zr alloy has advantages such as high mechanic strength [1], good thermal conductivity [2,3], and low thermal neutron absorption cross-section [4,5], making it widely used as a nuclear fuel cladding material. However, in the event of a loss-of-coolant accident (LOCA) in pressurized-water reactors (PWRs), the Zr-H₂O reaction becomes exacerbated, generating a significant amount of hydrogen and substantially increasing the risk of a “hydrogen explosion” [5,6]. After the Fukushima nuclear disaster, considerable attention has been directed towards accident-tolerant fuel (ATF) coatings [4,7], which have the potential to decelerate or even prevent the Zr-H₂O reaction. One of the most promising coating solutions within the ATF program is the metal Cr coating [5,8,9]. Cr is also oxidized in air or solution to form Cr₂O₃ passivation film. Cr₂O₃ has excellent oxidation resistance, which is the reason to choose Cr as coating material against high-temperature water and steam. In addition, the metal Cr coating not only offers protection

against high-temperature steam oxidation and chemical solution corrosion but also maintains the traditional fuel system.

However, despite its potential benefits, the practical application of Cr coating is hindered by several issues. For instance, under lithium borate solution conditions, there exists a significant potential difference between Zr and Cr ($\Delta E = 0.809$ V) [10]. The wear and tear of fuel rods and spacer grids can lead to cladding damage, exposing the coating-substrate interface to lithium borate solution [11,12], and causing galvanic corrosion with a large cathode and small anode, resulting in low corrosion resistance. Moreover, there is a serious issue of element interdiffusion within the Cr-coated Zr alloy cladding under a LOCA condition. On the one hand, the interdiffusion of elements between the Cr coating and Zr substrate results in the formation of a brittle Cr-Zr layer [13,14], which reduces the toughness of the coating-substrate system. On the other hand, at high temperatures, substrate elements diffuse into Cr coating grain boundaries, reacting with oxygen to form ZrO₂, creating rapid oxygen diffusion paths [15] and damaging the protective Cr coating. To address these issues, it is crucial to insert an appropriate insulation diffusion barrier between the Zr alloy cladding and the Cr coating.

Micro-arc oxidation (MAO) is a surface modification technology employing high-voltage discharges in an electrolyte solution to

* Corresponding author.

E-mail address: kepl@nimte.ac.cn (P. Ke).

¹ These authors contributed equally to this work.

form ceramic oxide coatings on metal surfaces [16–18]. In recent years, the MAO-coated Zr alloy was reported excellent corrosion resistance in a lithium borate solution and significantly improved steam oxidation resistance at temperatures below 1000 °C compared to the bare Zr alloy [19,20]. However, the MAO coating tends to fail at temperatures exceeding 1100 °C in steam environments. Nevertheless, the in-situ formed MAO coating exhibits a strong metallurgical bond [21] with the substrate, making it more suitable as an insulation diffusion barrier compared to CrN [22], TiC [23], and other insulation layers. Therefore, the application of MAO/Cr bilayer coating might be a promising approach to enhance the electrochemical corrosion resistance and high-temperature steam oxidation resistance of Zr alloy. In our previous works [24,25], we optimized the deposition parameters for both the MAO interlayer and Cr coating and preliminarily explored the steam oxidation resistance of the MAO/Cr-coated Zr alloy at 900 °C. A recent report by Xue et al. [26] also emphasized the MAO interlayer's role in inhibiting elemental interdiffusion between the Cr coating and Zr alloy, enhancing the steam oxidation resistance at 900–1100 °C. Notably, during a LOCA event, the temperature of the cladding can rapidly reach 1200 °C or higher. However, the steam oxidation resistance of MAO/Cr-coated Zr alloy at higher temperatures (>1100 °C) remains unclear. In addition, there is a lack of quantitative research on the electrochemical corrosion resistance of MAO/Cr-coated Zr alloy in lithium borate solution conditions.

In this paper, the MAO/Cr bilayer coating was fabricated on Zr alloy by a combination of micro-arc oxidation (MAO) and high-impulse-power magnetron sputtering (HiPIMS) surface treatments. The resistance to electrochemical corrosion and high-temperature steam oxidation of MAO/Cr-coated Zr alloys were characterized in a lithium borate solution and a 1200 °C steam environment, respectively. Furthermore, the influence mechanism of the MAO interlayer on the electrochemical corrosion and high-temperature steam oxidation behavior of MAO/Cr-coated Zr alloy was analyzed.

2. Experimental

2.1. Coating deposition

The cladding substrates utilized in this study were ZIRLO alloy plates [25,27], with dimensions measuring 15 mm (length) × 10 mm (width) × 2 mm (thickness). These substrates were initially polished up to #3000 grit with SiC sandpaper, followed by a 15-min ultrasonic cleaning in acetone, and then dried for further utilization.

The ZrO₂ MAO coating on the Zr substrate was prepared by a self-developed micro-arc oxidation (MAO) system, as shown in step 1 (Fig. 1), with the following parameters: 450 V voltage, 600 Hz frequency, and 15 % duty cycle for 3 min. Furthermore, the electrolyte, composed of 10 g/L Na₂SiO₃ and 2 g/L NaOH, was maintained at a constant temperature of around 30 °C during the MAO process.

The Cr coating was deposited on both bare and MAO-coated Zr substrates using a homemade high-impulse-power magnetron sputtering (HiPIMS) system, as shown in step 2 (Fig. 1). The vacuum chamber was evacuated to a base pressure below

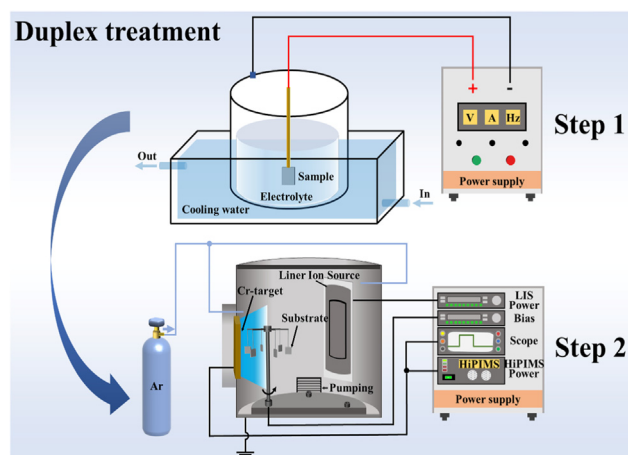


Fig. 1. Schematics of micro-arc oxidation (MAO) and high-impulse-power magnetron sputtering (HiPIMS) deposition systems.

2.8×10^{-5} Torr and then heated to 200 °C before deposition. Subsequently, the substrates underwent argon plasma etching to remove the adsorbed surface contaminants. During sputtering deposition, the substrates were hung on a rotating sample holder facing a high-purity Cr target (99.999 %) to improve the coating uniformity. Meanwhile, a DC-pulsed negative bias of –80 V was applied to enhance the bond strength between the coating and the substrate. The specific deposition parameters are listed in Table 1.

2.2. Electrochemical measurements and assessment of steam oxidation properties

The electrochemical tests (ASTM G59–97) were conducted using an electrochemical workstation (ModuLab XM ECS) in a solution containing 1200 mg/L H₃BO₃ and 2 mg/L LiOH. Before electrochemical testing, the coated samples needed to be encapsulated with epoxy resin. Specifically, the sample was placed in a mold, with copper leads accessed from the backside and secured with copper tape. Finally, the well-mixed epoxy resin and hardener were poured into the mold to seal the sides and back. After the resin had completely hardened, the sample was taken out for electrochemical corrosion testing. During the measurement, a three-electrode electrochemical system was employed. Specifically, the coated sample was designated as the working electrode, a platinum plate served as the counter electrode, and an Ag/AgCl electrode was used as the reference electrode. To achieve a stable open circuit potential (OCP) for the samples, we monitored the OCP continuously for two hours after immersing the samples in the electrolytic solution. The electrochemical impedance spectroscopy (EIS) was performed using a 10 mV amplitude at a frequency range of 10^5 – 10^{-2} Hz. The potentiodynamic polarization (PDP) test was conducted by starting at –0.5 V (vs. OCP) and increasing to +1 V (vs. OCP) at a scan rate of 1 mV/s. In addition, in order to gain insight into the long-term electrochemical corrosion behavior of the samples in lithium borate solution, a long-term immersion of 7

Table 1
Deposition parameters of the Cr coatings.

Method	Time (min)	Ar flow (sccm)	Pressure (mTorr)	Bias voltage (V)	Power supply				
					Power (kW)	Current (A)	Voltage (V)	Pulse width (μ s)	Duty ratio
Etching	15	40	2.5	–300	–	–	–	–	–
HiPIMS	420	50	1.8	–80	3.0	4.0	760	100	5 %

days was carried out, and the performance changes were characterized in situ.

The high-temperature steam oxidation tests were conducted on bare, Cr, and MAO/Cr coatings by a commercial thermogravimetric analyzer (TGA, SETARAM SETSYS, France). In particular, the samples were initially placed in the furnace with a continuous flow of high-purity argon to remove any remaining air. Afterward, the furnace temperature was rapidly increased from room temperature to 1200 °C at a rate of 15 °C/min and then held at 1200 °C for 30 and 90 min, respectively. Notably, steam was introduced into the furnace at 1200 °C, and maintained the relative humidity (RH) at 70 % for equipment safety during oxidation.

2.3. Characterizations

The crystal structures of the samples before and after steam oxidation were analyzed by X-ray diffraction (XRD, Bruker D8 Advance, Germany), employing Cu K α radiation ($\lambda = 0.154$ nm) and a 0.02° step in the conventional θ – 2θ configuration. Their morphologies and elemental compositions were characterized using a scanning electron microscope (SEM, Verios G4 UC, USA) with energy-dispersive X-ray spectrometry (EDS). The phase components were determined through electron backscatter diffraction (EBSD), which was equipped with the SEM system. Before EBSD characterization, all cross-sectional samples underwent Ar-ion milling. Additionally, the polished oxidized samples were immersed in a mixed acid corrosion solution (1.0 % HF+1.5 % HCl +2.5 % HNO $_3$ +95 % H $_2$ O) for 5–10 s, and their metallographic organization was examined using an optical microscope (OM, NMM-800RF, China). The adhesion strength of the MAO/Cr coating and the Cr coating was evaluated by the Revetest scratch test system (CSM). The applied load increased linearly from 0 N to 50 N as the scratch distance extended from 0 mm to 5 mm.

3. Results and discussion

3.1. Structure and composition of coating

Fig. 2 shows the difference in the cross-sectional morphology of the Cr coating and MAO/Cr coating. As shown in Fig. 2(a) and (c), the single Cr coating exhibits a uniform and dense columnar microstructure, which can be attributed to the high plasma density and low plasma energy of the HiPIMS discharge with a Cr target [28,29]. In contrast, the MAO/Cr bilayer coating consisting of the top Cr layer (exhibiting a compact columnar microstructure) and the MAO interlayer (porous and containing microcracks) shows relatively poor uniformity (Fig. 2(d) and (f)). In fact, the micro-arc oxidation process involves a breakdown discharge [16,30], resulting in the formation of micropores on the surface of the MAO layer and an increase in surface roughness. Moreover, the rapid cooling of the melt-in solution during the micro-arc oxidation process can generate thermal stress, potentially resulting in the development of microcracks within the MAO layer. The grain-size statistical results for the top Cr layer in Cr and MAO/Cr coatings are presented in Fig. 2(g) and (h). It should be noted that the average grain size in Fig. 2(f) is 21.5 % smaller than that in Fig. 2(c). This difference in grain size could be attributed to the greater number of surface defects present in the MAO layer compared to the Zr substrate. These defects increased the nucleation sites for Cr grains during HiPIMS deposition, thereby promoting grain refinement of the Cr top layer. Additionally, the EDS results (Fig. 2(b) and (e)) indicate that both the single Cr coating and the MAO/Cr bilayer coating have a high purity of the top Cr layer, and the composition of the MAO interlayer layer (with an atomic ratio of Zr to O approximately 1:2) corresponds to ceramic ZrO $_2$.

Fig. 3 shows the XRD patterns and corresponding texture coefficients of the Cr and MAO/Cr coatings. The diffraction peaks in Fig. 3(a) were consistent with body-center cubic (BCC) Cr, while no Zr or ZrO $_2$ diffraction peaks were observed. This was possible because the penetration depth of the X-ray used for the diffraction analysis was smaller than the thickness of the top Cr layer. To further determine the phase composition of the MAO layer, we performed an extra XRD experiment (Fig. S1) on the MAO-coated Zr alloy. The result confirmed that the phases present in the MAO layer were monoclinic zirconia (M-ZrO $_2$) and tetragonal zirconia (T-ZrO $_2$), consistent with the findings from the EDS analysis. In addition, there were distinct differences in crystal orientation between Cr coating and MAO/Cr coating. Specifically, the Cr coating displayed a strong diffraction peak at (110), while MAO/Cr coating exhibited strong diffraction peaks at both (110) and (200). To quantitatively identify the crystal orientation of Cr and MAO/Cr coatings, the texture coefficient (TC) was defined using the following formula [31]:

$$TC = \frac{I_{(hkl)}/I_{0(hkl)}}{\sum [I_{(hkl)}/I_{0(hkl)}]} \quad (1)$$

where “ $I_{0(hkl)}$ ” and “ $I_{(hkl)}$ ” represent the diffraction peak intensity at the (hkl) crystal plane in the standard PDF card and the actual coating, respectively. Fig. 3(b) illustrates the calculation results of specific texture coefficients for Cr and MAO/Cr-coatings. The Cr coating was assigned the (110) texture with a texture coefficient of 81 %, whereas the MAO/Cr coating was assigned the (200) texture with a texture coefficient of 83 %. For the BCC (Body-Centered Cubic) Cr grains, the (110) crystal plane exhibited the lowest surface energy [25,32], while the (200) crystal plane demonstrated the lowest strain energy [33]. It should be noted that the HiPIMS technique can promote the lateral growth of Cr grains with a low-surface-energy orientation, thereby enhancing the possibility of forming a strong (110) texture [25]. However, defects in the MAO interface layer can lead to stress concentration, which promotes the metal Cr atoms to preferentially select the (200) crystal plane with low-strain-energy for crystallization growth. Thus, the MAO/Cr coating exhibited a stronger (200) texture compared to the Cr coating.

3.2. Long-term electrochemical corrosion measurement

The OCP evolutions of the Zr substrate, Cr coating, and MAO/Cr coating immersed in lithium borate solution for 7 d are shown in Fig. 4.

The initial OCP of the Zr substrate was –0.223 V, which changed to –0.205 V after 1 d of immersion. It then continued to rise monotonically, increasing to –0.18 V after 7 d. This indicated that the Zr substrate was gradually oxidized/passivated during prolonged immersion, causing a slow increase in OCP. Unlike this, the OCPs of the MAO/Cr coating (0.153–0.156 V) and Cr coating (0.011–0.015 V) remained relatively stable throughout the immersion cycle. This meant that both coatings could be stabilized in lithium borate solution and prevented from penetrating the solution into the Zr interface during long-term immersion. Notably, the OCP values of the MAO/Cr coating were consistently much higher than those of the Cr coating and Zr substrate. A high potential typically indicates low susceptibility to corrosion [34]. Therefore, it could be hypothesized that the MAO/Cr coating had the lowest corrosion tendency in all samples during long-term immersion, this phenomenon can be explained in two ways. First, as shown in the EBSD results (Fig. 2), the grain size of the Cr top layer of the MAO/Cr coating was much smaller than that of the Cr coating. As the grain size decreases, the active sites of the metal increase (such as grain boundaries), which helps the passivation system

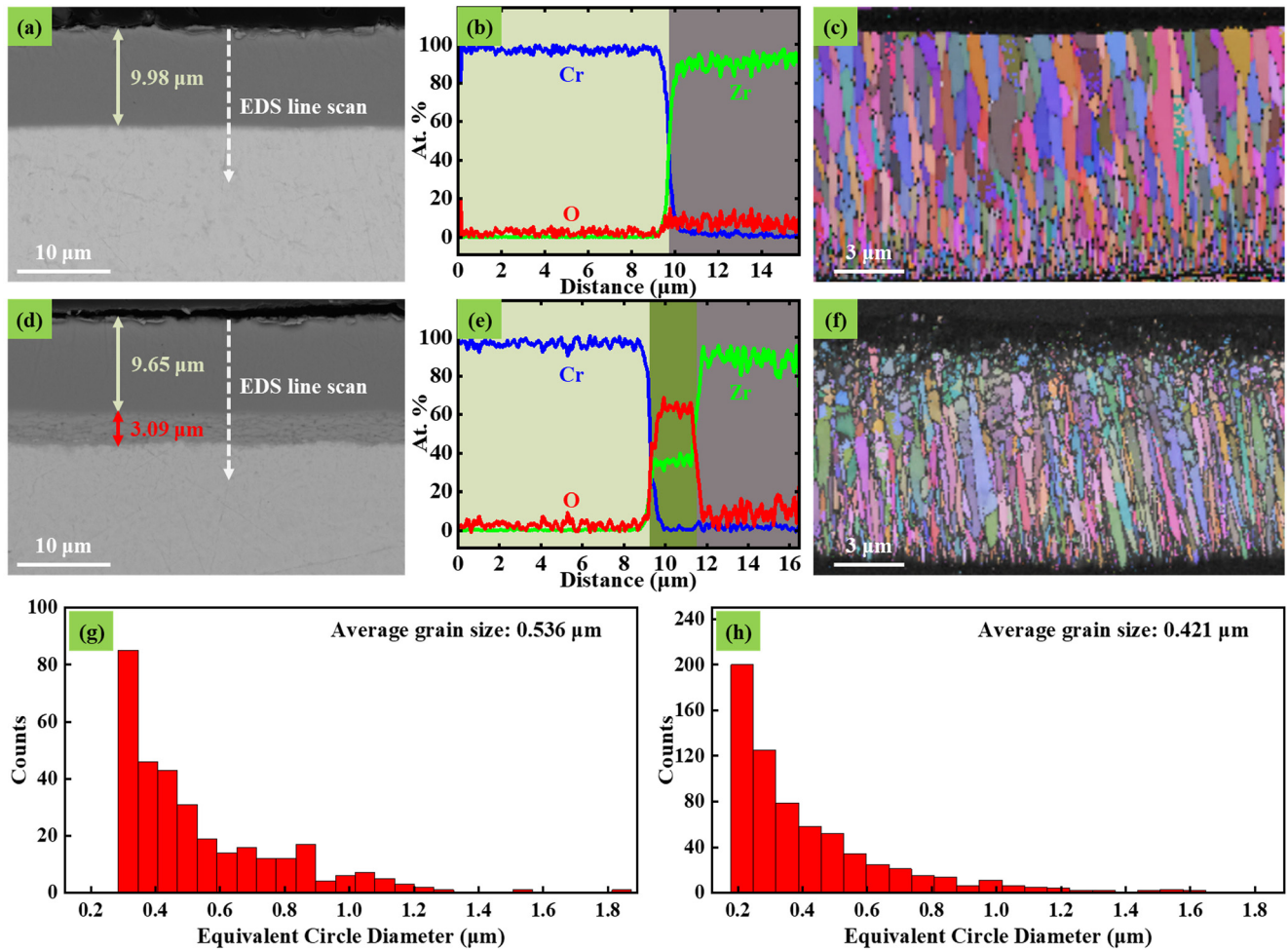


Fig. 2. Cross-sectional SEM images (a, d) and EDS line scanning composition profiles (b, e) of the Cr coating and MAO/Cr coating. Corresponding EBSD patterns for the top Cr layer in (a) and (d) are shown in (c, g) and (f, h), respectively.

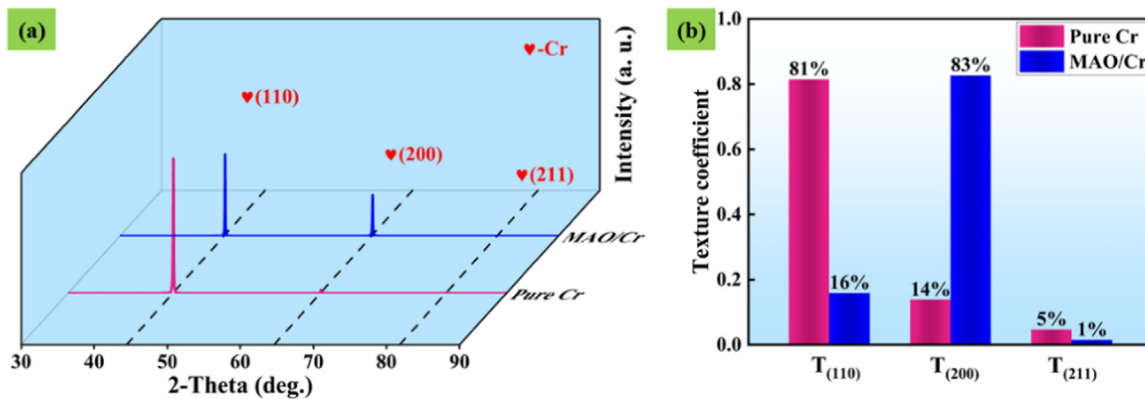


Fig. 3. XRD patterns (a) and texture coefficients (b) of Cr and MAO/Cr coatings.

to form a protective passivation film. Cr is a typical passivation system, so grain refinement will promote the formation of passivation films, which can explain the electrochemical test results of MAO/Cr coating having higher OCP than Cr coating. Moreover, besides the Cr top layer, the difference in material composition (Zr-MAO vs. Zr) could also be the reason for the difference in OCP between the two.

To further evaluate the corrosion resistance of the samples, the EIS of the Zr substrate, Cr coating, and MAO/Cr coating were

monitored over time and the results are shown in Fig. 5. In the Nyquist plots (Fig. 5(a₁-c₁)), it was observed that the MAO/Cr coating had a larger capacitive arc radius compared to the Cr coating and Zr substrate during all immersion cycles. Usually, a larger radius of the capacitive arc in the Nyquist plot means better corrosion resistance [35]. Therefore, it could be tentatively concluded that the MAO/Cr coating exhibited the best corrosion resistance among all the samples. Besides Nyquist plots, Bode plots (including Bode phase angle and Bode impedance)

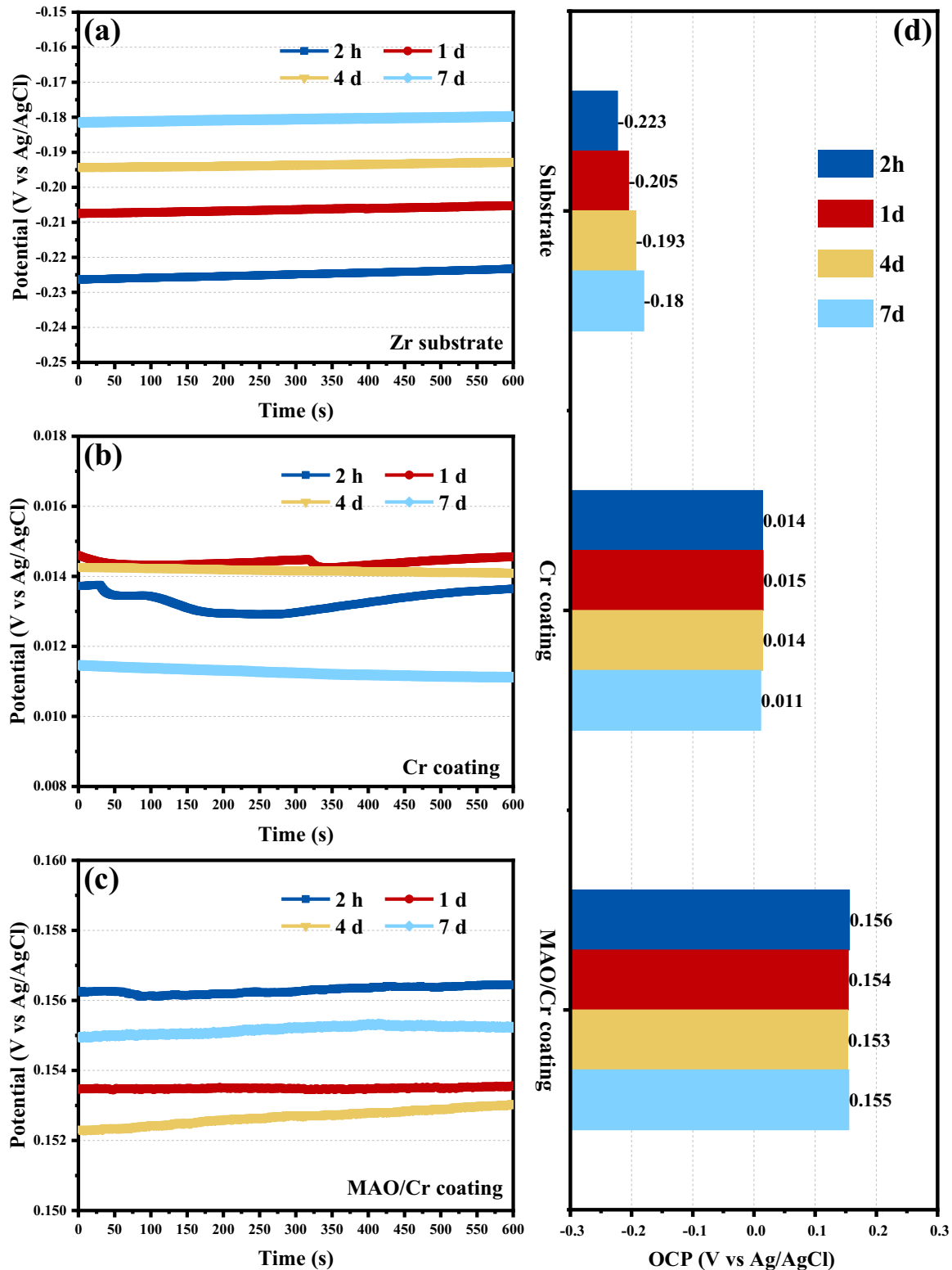


Fig. 4. (a–c) OCP evolution and (d) specific stabilization values of the Zr substrate, Cr coating, and MAO/Cr coating for long-term immersion in lithium borate solution.

also give critical information about the corrosion resistance of samples.

In Fig. 5(a₂–c₂), it was observed that the phase angle of the MAO/Cr coating in the high-frequency region (10⁵–10³ Hz) was always maintained at high values, indicating an excellent barrier to solution penetration [36]. In addition, in the Bode impedance

plots (Fig. 5(a₃–c₃)), the impedance modulus ($|Z|_{0.01 \text{ Hz}}$) of the MAO/Cr coating ($\sim 5.12 \times 10^6 \Omega \text{ cm}^2$) was much higher than that of the Cr coating ($\sim 2.53 \times 10^6 \Omega \text{ cm}^2$) and the Zr substrate ($\sim 1.51 \times 10^6 \Omega \text{ cm}^2$). This also demonstrated that the MAO/Cr coating presented excellent barrier properties and effectively avoided the penetration of the solution into the Zr sub-

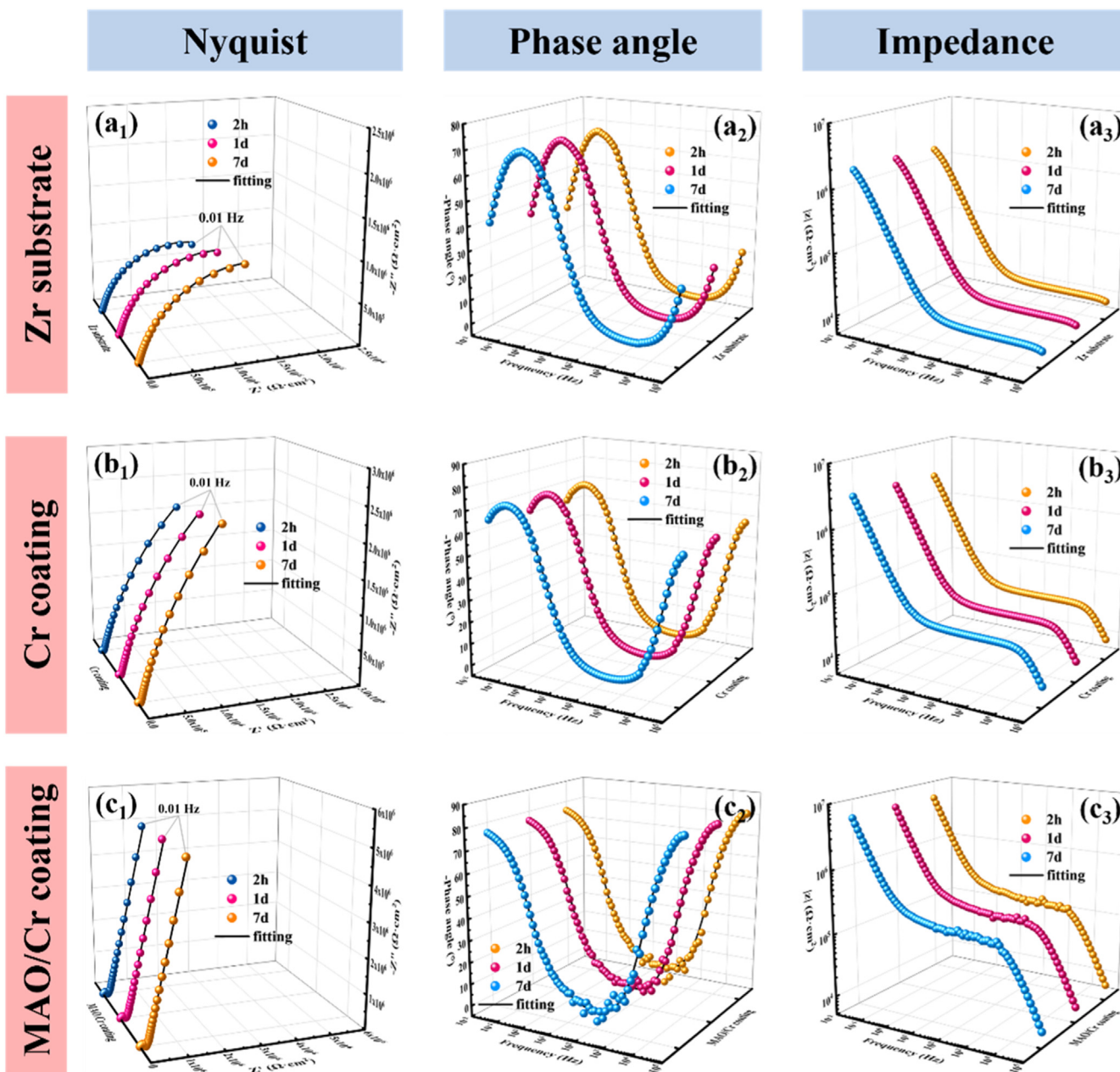


Fig. 5. EIS evolution of the (a₁–a₃) Zr substrate, (b₁–b₃) Cr coating, and (c₁–c₃) MAO/Cr coating for long-term immersion in lithium borate solution.

strate. In addition, there was no significant change in the EIS (both Nyquist and Bode) results of the MAO/Cr coating after prolonged immersion (7 d). This meant that the MAO/Cr coating provided excellent electrochemical corrosion protection for the Zr substrate at ambient temperature.

The EIS results were further fitted by ZView software to quantify the evolution of the corrosion properties during long-term immersion. The equivalent circuit model used for EIS fitting is shown in the inset of Fig. 6, where R_s , R_c , and R_{ct} are the solution resistance, the Cr layer resistance, and the charge transfer resistance at the Cr layer-Zr substrate interface, respectively. The R_c of the Zr substrate sample is assigned to the passive film. The Warburg impedance (W) is introduced in the MAO/Cr coating sample to describe the diffusion process of corrosive species through the MAO interlayer defects. The constant phase element (CPE) is used to represent the capacitive characteristics of the Cr layer surface (CPE_c) and the electrical double layer between the Cr layer and the Zr

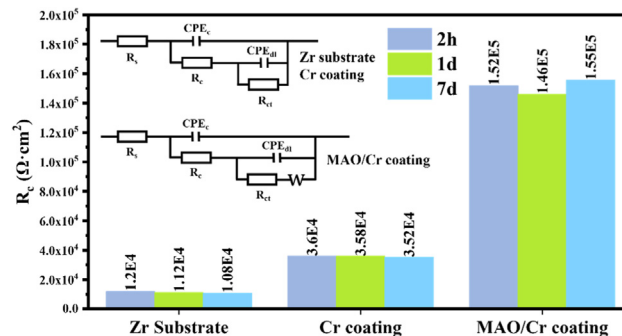


Fig. 6. R_c obtained by EIS fitting (Inset: equivalent circuit model).

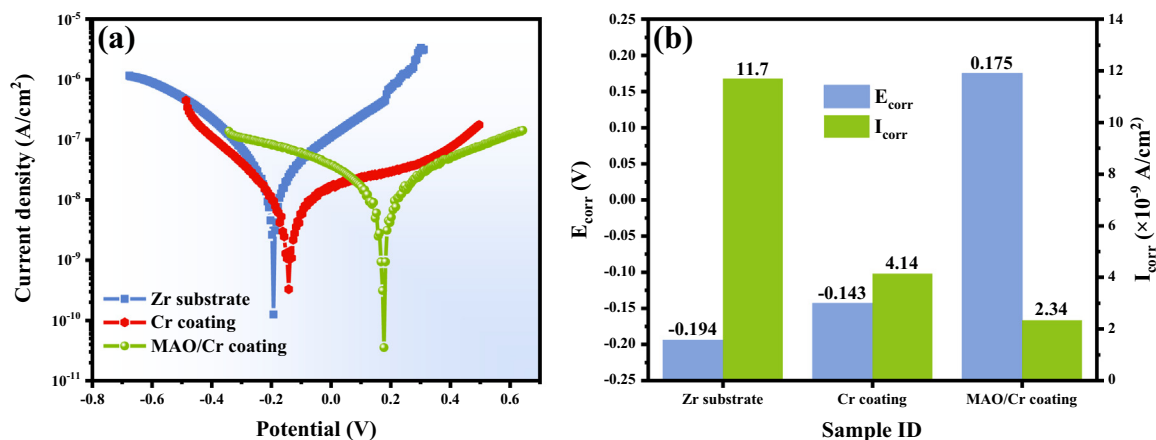


Fig. 7. (a) PDP curves, (b) E_{corr} and I_{corr} of the Zr substrate, Cr coating, and MAO/Cr coating after 7d immersion in lithium borate solution.

substrate (CPE_{dl}). It is worth noting that the thickness of the Cr top layer was as high as $\sim 10 \mu\text{m}$ for both the Cr coating and the MAO/Cr coating. In addition, combined with the OCP results of long-term immersion, it can be determined that the corrosion solution did not break through the Cr layer; thus, the difference in the surface passivation properties of the three samples was the main factor affecting the corrosion resistance. Therefore, we focused on discussing R_c (resistance of Zr substrate passive film or Cr layer). As shown in Fig. 6, the R_c values of both the MAO/Cr coating and the Cr coating were higher than those of the Zr substrate during long-term immersion. It showed that both coatings could stabilize and enhance the electrochemical corrosion resistance of the Zr substrate. Moreover, the R_c of the MAO/Cr coating ($\sim 1.5 \times 10^5 \Omega \text{cm}^2$) was about an order of magnitude higher than that of the Cr coating ($\sim 3.6 \times 10^4 \Omega \text{cm}^2$), indicating that the surface passivation ability of the MAO/Cr coating was more significant. This was attributed to the surface defects of the MAO interlayer increasing the nucleation sites of Cr grains, so the Cr top layer of the MAO/Cr coating had finer grains and was more likely to form a protective Cr_2O_3 passive film.

The PDP tests were performed on the Zr substrate, Cr coating, and MAO/Cr coating after 7d of immersion, the results are shown in Fig. 7. It was not difficult to see that after prolonged immersion, the MAO/Cr coating (0.175 V, 2.34×10^{-9} A/cm²) still possessed the highest self-corrosion potential (E_{corr}) and the lowest self-corrosion current density (I_{corr}) compared to the Cr coating (-0.143 V, 4.14×10^{-9} A/cm²) and the Zr substrate (-0.194 V, 11.7×10^{-9} A/cm²). The electrochemical protection efficiencies of the MAO/Cr and Cr coatings on the Zr substrate were 80 % and 65 %, respectively, indicating that the MAO ceramic interlayer significantly enhanced the protective ability of the Cr coating. This phenomenon emphasized the superior corrosion resistance of the MAO/Cr coating, which was also consistent with the results of the OCP and EIS tests mentioned above. In addition, to evaluate the protection efficiency and adhesion strength of the two coatings before immersion, we performed PDP tests (Fig. S2) and adhesion strength tests (Fig. S3) on the as-deposited samples. The results demonstrated that the MAO/Cr coating (1.72×10^{-10} A/cm²) had the lowest I_{corr} compared to the Cr coating (3.66×10^{-10} A/cm²) and Zr substrate (13.4×10^{-10} A/cm²), and its protection efficiency for the substrate was 14 % higher than that of the Cr coating (73 %). However, the I_{corr} before immersion was lower than after for all samples, indicating that the solution had not yet entered the coating. The scratch test results showed that the adhesion strengths of MAO/Cr coating with Cr top layer (~ 25 N) and Cr coating are higher than 20 N, which can satisfy long-term use in most engineering fields. It is interesting to note that the Cr coating was not

observed to crack/spall during sliding and was only pressed into the substrate or extruded, which may be due to the lack of support capacity of the Zr substrate. In short, the electrochemical results revealed that incorporating the MAO ceramic interlayer between the Cr coating and the Zr substrate could confer exceptional and durable electrochemical corrosion resistance in lithium borate solution.

3.3. High-temperature steam oxidation

The high-temperature steam oxidation tests were performed using a commercial thermogravimetric analyzer (TGA). Before the oxidation process, the total surface areas (including the top, bottom, and four sides) of the Zr substrate, Cr coating, and MAO/Cr coating were measured respectively. Subsequently, the TGA test was performed on each sample, and finally, the oxidation weight gain per unit area was obtained. Fig. 8 illustrates the oxidation kinetics curves of the Zr substrate, Cr, and MAO/Cr coatings in a steam environment at 1200 °C for 90 min. It should be noted that the Zr substrate demonstrated poor oxidation resistance. Specifically, the weight gain rate of the Zr substrate increased rapidly over time during the initial stage, reaching its peak at 17.5 min, and subsequently decreasing to a stable state (Fig. 8(a)).

In contrast, both Cr and MAO/Cr coatings exhibited relatively lower weight gain rates throughout the entire oxidation process (Fig. 8(b)). This can be attributed to both types of coatings forming a passive film [37] during the initial oxidation, effectively inhibiting the penetration of external corrosive medium into the alloy. In addition, the MAO/Cr bilayer coating consistently displayed a lower weight gain rate compared to the Cr coating during the oxidation process. The decreased rate of weight gain for the MAO/Cr bilayer can be attributed to the synergistic effect of the refined Cr grains and the MAO diffusion barrier in impeding oxidation. Ultimately, after oxidation at 1200 °C for 90 min, the MAO/Cr bilayer coating displayed a weight gain approximately 65.9 % and 34.9 % lower than that of the bare Zr alloy and Cr coating, respectively (Fig. 8(c)). Therefore, the MAO/Cr bilayer structure demonstrated significantly enhanced resistance to steam oxidation at 1200 °C compared to both the single-layer Cr coating structure and the bare Zr alloy.

Fig. 9 shows the XRD results of both Cr and MAO/Cr coatings after oxidation at 1200 °C for 30 min and 90 min, respectively. After exposing the Cr and MAO/Cr coatings to steam at 1200 °C for either 30 min or 90 min, obvious diffraction peaks of Cr_2O_3 and Cr were observed in both coatings, indicating that the main oxidation product formed was Cr_2O_3 . Interestingly, the Cr and MAO/Cr coatings exhibited a strong Cr (110) diffraction peak while lacking

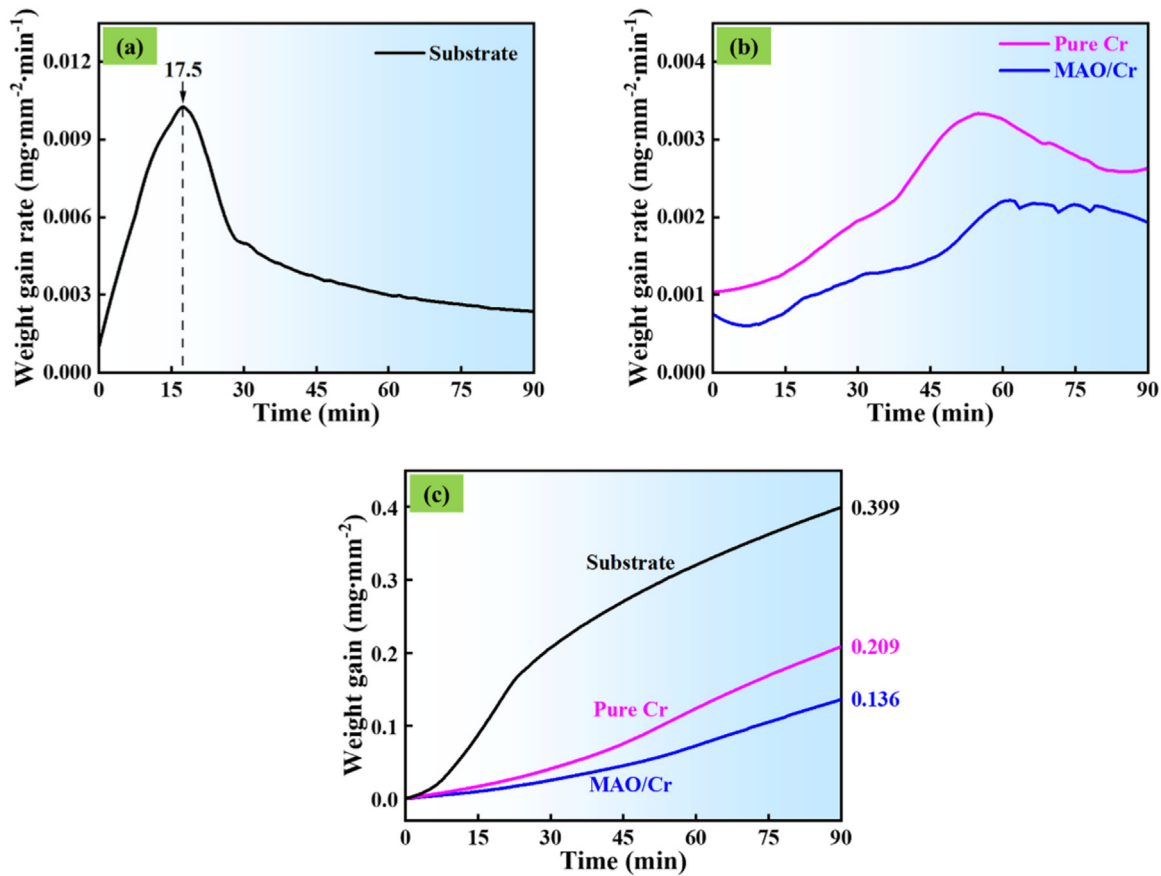


Fig. 8. (a–c) Oxidation kinetics curves of bare, Cr, and MAO/Cr coatings in 1200 °C steam environment.

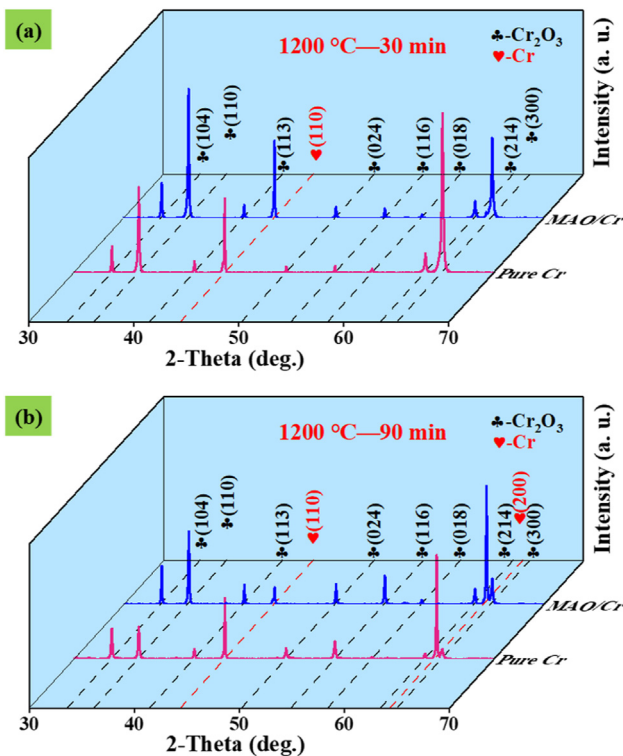


Fig. 9. XRD results of Cr and MAO/Cr coatings after oxidation at 1200 °C for 30 min (a) and 90 min (b).

a Cr (200) diffraction peak after undergoing oxidation at 1200 °C for 30 min.

However, following oxidation at 1200 °C for 90 min, both coatings displayed a strong Cr (110) diffraction peak and an even stronger Cr (200) diffraction peak. In fact, the reduction of compressive residual stress generated by the recovery effect [38] after high-temperature treatment can promote the recrystallization growth of Cr coatings along the lowest surface-energy (110) crystal plane. However, with prolonged oxidation, the Cr₂O₃ phase may be reduced to a new Cr phase exhibiting a (200)-preferred orientation in both coating samples. This reduction phenomenon [14,26] has been reported by several researchers.

Fig. 10 shows the difference in cross-sectional morphologies of bare, Cr, and MAO/Cr coatings after oxidation at 1200 °C for 30 min. After oxidation, all three samples displayed a distinct hierarchical structure. Combining with the EDS results listed in Table 2, the oxidized bare Zr alloy consisted of the following layers, arranged from outermost to innermost: a ZrO₂ scale with slender columnar crystals, an oxygen-stable α-Zr(O) layer with coarse columnar crystals, and a Prior β-Zr layer with a lath structure. Kim et al. [39] proposed that in a high-temperature steam environment, external oxygen atoms can diffuse through the ZrO₂ scale into the Zr alloy, causing a phase transformation from β-Zr to α-Zr in the near-surface region of the alloy and resulting in the formation of an oxygen-stable α-Zr(O) layer. In contrast, the oxidized Cr and MAO/Cr coating samples displayed a notably diverse multi-layered structure, including a Cr₂O₃ scale, a residual Cr layer, a Cr_xZr_y(O) interdiffusion layer, an oxygen-stabilized α-Zr(O) layer, and a Prior β-Zr layer from the surface to the core. It should be noted that the oxidized Cr and MAO/Cr coating samples both showed Cr₂O₃ scales less than 10 μm thick, approximately 1/6 thinner than the

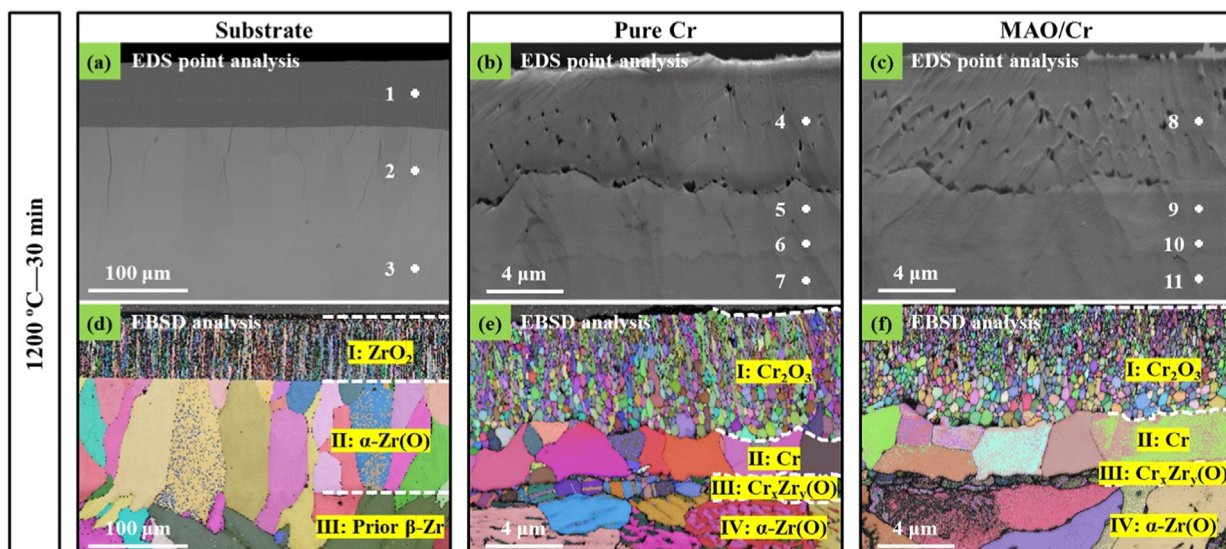


Fig. 10. Cross-sectional SEM images and corresponding EBSD Euler images of bare (a, d), Cr (b, e) and MAO/Cr (c, f) coatings oxidized at 1200 °C for 30 min. The compositions of the areas labeled as numbers in (a), (b) and (c) are listed in Table 2.

Table 2
Chemical compositions (at.%) of the EDS point analysis in Fig. 10.

	Substrate			Pure Cr				MAO/Cr			
	1	2	3	4	5	6	7	8	9	10	11
Zr	33.6	74.2	79.2	0.3	0.4	19.3	59.4	0.3	0.5	21.7	63.7
Cr	0.0	0.0	0.0	42.9	97.4	69.4	15.2	43.2	96.2	70.8	11.9
O	66.4	25.8	20.8	56.8	2.2	11.3	25.4	56.5	3.3	7.5	24.4

ZrO₂ scale observed on the oxidized bare Zr alloy under the same high-temperature steam conditions. One possible reason is that external oxygen atoms can easily pass through slender grain boundaries within columnar ZrO₂ crystals, leading to accelerated oxidation through short-circuit diffusion. Conversely, the Cr₂O₃ scale, composed of fine equiaxed crystals, effectively inhibits the diffusion of external oxygen atoms to the core, thus reducing the oxidation rate. Meanwhile, numerous micro-pores were observed in the Cr₂O₃ scale. These pores can be attributed to the further oxidation of Cr₂O₃ into volatile compounds, such as CrO₃ and CrO₂(OH)₂ [40], which readily escape from the surface at high temperatures. In addition, during the oxidation process, both the Cr and MAO/Cr coatings exhibited a columnar-to-equiaxed transition (CET) in their top Cr layers. Interestingly, the oxidized MAO/Cr coating displayed larger equiaxed Cr crystals than the oxidized Cr coating. In fact, the grain size of Cr crystals within the oxidized Cr and MAO/Cr coating samples was closely connected to the recrystallization process. Unlike the (110)-textured Cr coating, the top Cr layer in the (200)-textured MAO/Cr coating had reduced lattice distortion due to lower internal strain, hindering recrystallization nucleation and leading to coarser Cr grains. In addition, the MAO/Cr coating exhibited a significantly thinner Cr_xZr_y(O) interdiffusion layer than the Cr coating after oxidation, suggesting that the MAO layer partially inhibits interdiffusion between the Zr alloy and the top Cr coating at high temperatures.

To further assess the oxygen permeation resistance of bare, Cr and MAO/Cr coatings, we conducted cross-sectional optical microscopy (OM) analysis after exposing them to 1200 °C steam for 30 min, as well as chemical corrosion (Fig. 11). Compared to Cr and MAO/Cr coating samples, the bare Zr alloy exhibited a significantly thicker α-Zr(O) layer, confirming that the ZrO₂ scale was less efficient in hindering external oxygen diffusion to the substrate than the Cr₂O₃ scale. In addition, the EDS mappings (Fig. 11(d, e))

revealed that the grain boundaries within the residual Cr layer contained precipitates enriched with Zr. In our previous studies [41,42], we identified these precipitates as ZrO₂ grains through TEM and EBSD characterization. These ZrO₂ grains were interconnected, forming a network that facilitated rapid diffusion paths for oxygen, ultimately leading to the formation of a near-surface α-Zr(O) layer. It should be emphasized that the oxidized MAO/Cr coating showed less rapid diffusion pathways for oxygen, which can be attributed to the decreased grain boundaries in the residual Cr layer compared to the oxidized Cr coating sample. Combined with the oxidation kinetics curves in Fig. 8, the reduction in grain boundaries within the residual Cr layer significantly improved the oxygen diffusion-blocking capability of the MAO/Cr coating in a high-temperature steam environment.

Considering the outstanding oxidation resistance exhibited by Cr and MAO/Cr coatings in a high-temperature steam environment, the anti-oxidation properties of the bare, Cr, and MAO/Cr coatings were further compared and evaluated after steam oxidation at 1200 °C for 90 min. As shown in Fig. 12(a) and (d), the bare Zr alloy suffered severe oxidative damage, and obvious micro-cracks were observed in its cross-section. Moreover, extending the oxidation time from 30 to 90 min significantly increased the grain size and changed the shape of the α-Zr(O) layer in the bare Zr alloy from columnar to equiaxed crystals, attributed to the Oswald ripening [43] during high-temperature recrystallization. Cross-sectional images of Cr and MAO/Cr coating samples oxidized for 90 min are presented in Fig. 12(b, e) and (c, f), indicating a reduction in Cr₂O₃ scale thickness and an increase in the Cr layer thickness compared to the 30-min oxidation period. This phenomenon can be attributed to the fact that, once the Cr₂O₃ scale reached its maximum thickness, it was subsequently reduced by the underlying Zr substrate [14], as previously reported by Han et al. It was noteworthy that the weight gains of Cr coating and MAO/Cr coat-

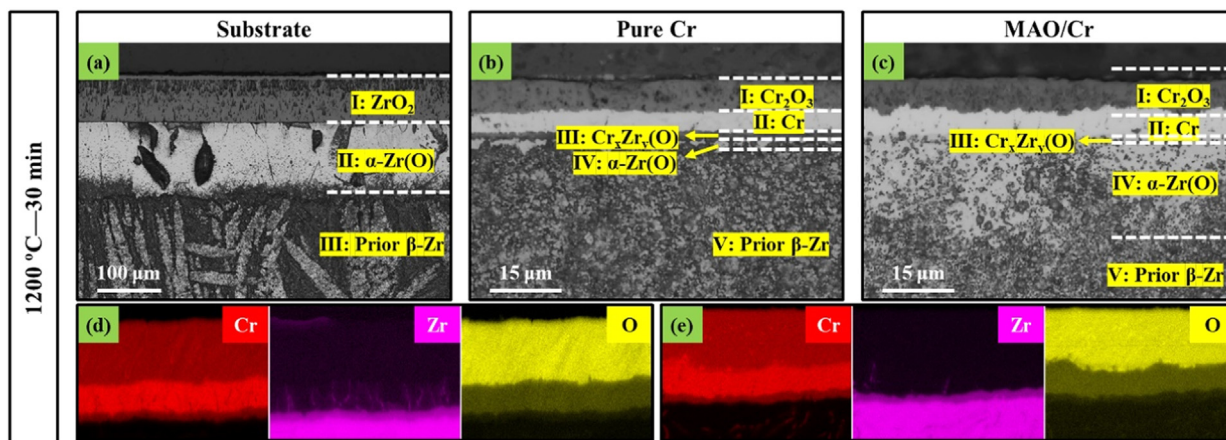


Fig. 11. Cross-section OM images (a, b, c) of bare, Cr, and MAO/Cr coatings oxidized at 1200 °C for 30 min, followed by chemical corrosion. Corresponding EDS mappings for the oxidized Cr, and MAO/Cr coatings are shown in (d) and (e), respectively.

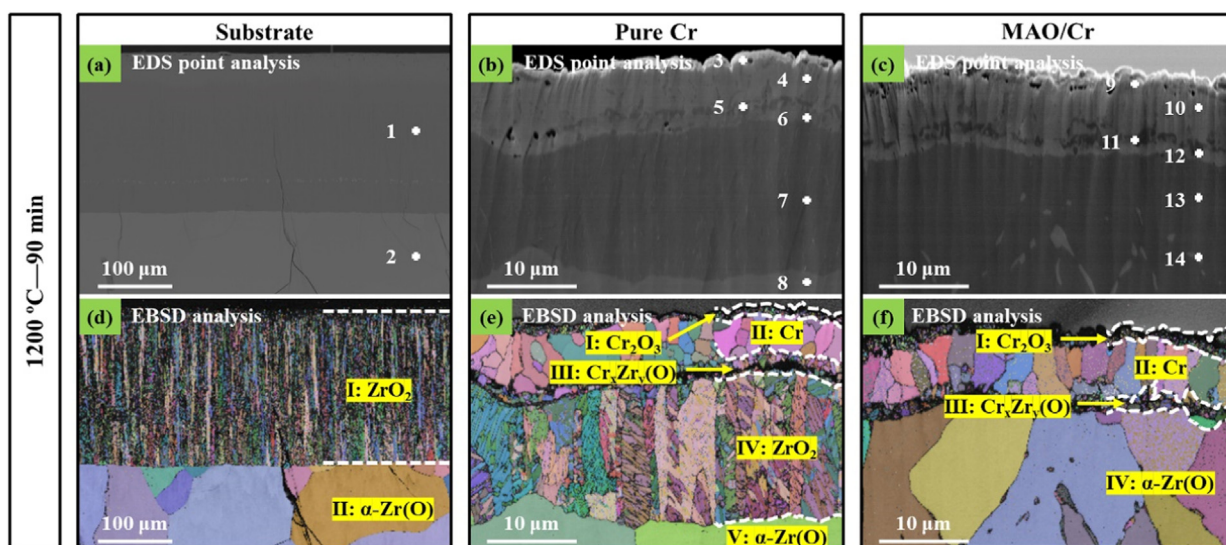


Fig. 12. Cross-sectional SEM images and corresponding EBSD Euler images of bare (a, d), Cr (b, e) and MAO/Cr (c, f) coatings oxidized at 1200 °C for 90 min. The compositions of the areas labeled as numbers in (a–c) are listed in Table 3.

Table 3
Chemical compositions (at.%) of the EDS point analysis in Fig. 12.

	Substrate		Pure Cr					MAO/Cr						
	1	2	3	4	5	6	7	8	9	10	11	12	13	14
Zr	35.3	78.8	0.3	0.4	34.7	23.2	36.6	70.8	0.2	0.3	24.8	38.6	71.2	59.4
Cr	0.0	0.0	40.2	97.2	50.2	37.4	0.2	0.2	41.3	97.6	35.4	55.2	0.3	29.3
O	64.7	21.2	59.5	2.4	15.1	39.4	63.2	29.0	58.5	2.1	39.8	6.2	28.5	11.3

ing suddenly increased (Fig. 8(c)) after approximately 40 min. One possible reason was that the protective Cr₂O₃ scale began to decrease at this point, and the newly-formed reduced Cr layer could not effectively prevent the permeation of outside oxygen.

Furthermore, the EDS point analysis (Table 3) confirmed the oxidized Cr-coated sample formed a coherent ZrO₂ layer, in contrast to the oxidized MAO/Cr-coated sample, highlighting the superior high-temperature steam oxidation resistance of the MAO/Cr coating over the Cr coating. Additionally, a multitude of chromium-rich exudates were observed in the α-Zr(O) layer of the oxidized MAO/Cr-coated sample, attributable to the diffusion of Cr from the coating into the alloy, indicating the coating was on the verge of failure.

Fig. 13 shows the cross-section OM images of bare, Cr, and MAO/Cr coatings oxidized at 1200 °C for 90 min, followed by chemical corrosion. In contrast to the oxidized coating samples, the oxidized bare Zr alloy displayed a thicker ZrO₂ scale and more defects, highlighting the need for anti-oxidation coatings to ensure the safety and reliability of Zr alloy cladding under LOCA conditions. In addition, the α-Zr(O) layer in the Cr coating sample was thicker than in the MAO/Cr coating sample after oxidation for 90 min, in contrast to the situation observed after oxidation for 30 min, where the α-Zr(O) layer in the Cr coating sample was smaller than in the MAO/Cr coating sample. This difference can be attributed to the superior oxygen diffusion-blocking capability of the MAO/Cr coating compared to the Cr coating, despite the even-

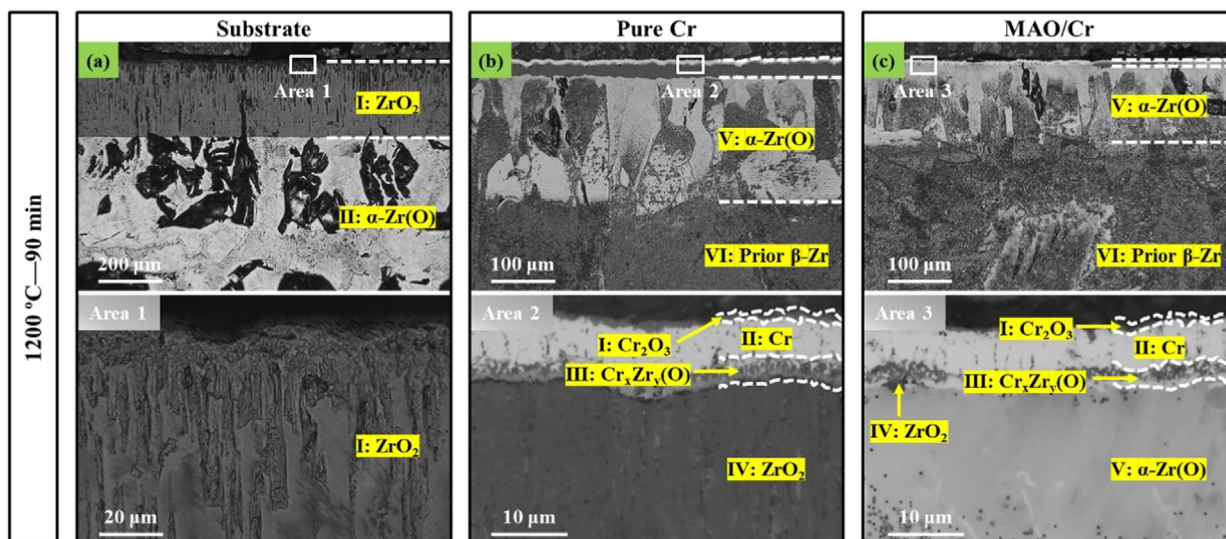


Fig. 13. Cross-section OM images of bare, Cr and MAO/Cr coatings oxidized at 1200 °C for 90 min, followed by chemical corrosion.

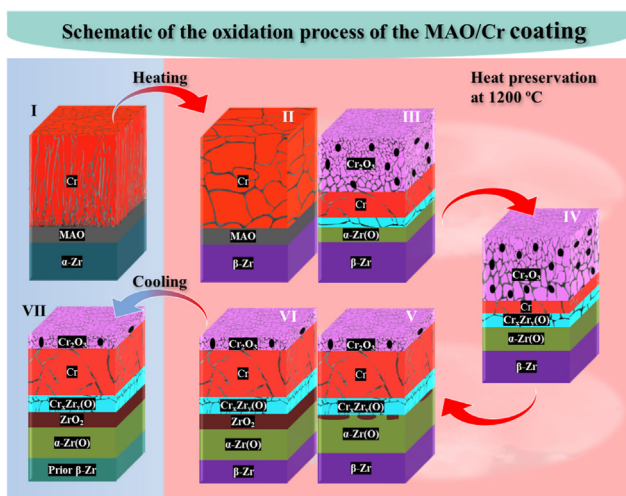


Fig. 14. Schematic of the oxidation process of the MAO/Cr coating on Zr substrate at 1200 °C in a steam environment.

tual degradation of the MAO interface layer in high-temperature steam environments.

Fig. 14 illustrates the oxidation process of the MAO/Cr-coated Zr alloy in a steam environment at 1200 °C. As the temperature increased to 1200 °C, the crystal structure of the Zr substrate shifted from α -Zr (I) with a hexagonal close-packed (HCP) structure to β -Zr (II) with a body-centered cubic (BCC) structure. At the same time, the top Cr layer underwent a transition from slender columnar crystals to larger equiaxed crystals, driven by recrystallization growth at high temperatures. During the short-term oxidation process from Stage II to Stage IV at 1200 °C, the Cr_2O_3 scale thickened, the residual Cr layer thinned over time, and a $\text{Zr}_x\text{Cr}_y(\text{O})$ layer formed due to element interdiffusion between Zr alloy and MAO/Cr coating. Besides, the oxygen element easily diffused from the MAO interlayer into the Zr substrate due to the temperature exceeding 900 °C [10]. This diffusion resulted in the degradation of the MAO interlayer and a transition in the near-surface Zr substrate from β -Zr (II) to the α -Zr(O) (III). After the thickness of the residual Cr layer reached the minimum, with extended oxidation time, the protective Cr_2O_3 scale gradually diminished as it was reduced by the underlying Zr substrate, newly forming a non-protective re-

duced Cr layer and a ZrO_2 layer between the $\text{Cr}_x\text{Zr}_y(\text{O})$ and α -Zr(O) layers (V). Furthermore, the thinning of the protective Cr_2O_3 scale facilitated external oxygen diffusion to the substrate, thickening both the ZrO_2 layer and the α -Zr(O) layer (VI). The oxidized MAO/Cr-coated Zr alloy was then cooled to room temperature, inducing a transition of the high-temperature β -Zr phase into the α -Zr phase, commonly denoted as "Prior β -Zr" (VII) to distinguish it from the α -Zr phase existing before oxidation.

4. Conclusion

In this study, we successfully fabricated MAO/Cr bilayer coating on Zr alloy via a combination of MAO and HiPIMS surface treatments. The corrosion resistance to electrochemical and high-temperature steam of the bare, Cr, and MAO/Cr coatings was comparatively studied. The results showed that the MAO interlayer could refine the grain size of the Cr top layer, and promote the growth of passive film, thus improving its electrochemical corrosion resistance in lithium borate aqueous solution. Furthermore, under simulated LOCA conditions with 1200 °C steam, the MAO interlayer gradually degraded with increasing oxidation time. Nevertheless, after oxidation for 90 min, the MAO/Cr bilayer coating exhibited a weight gain roughly 65.9 % lower than the bare Zr alloy and 34.9 % lower than the Cr coating. This can be attributed to the MAO interlayer inhibiting element interdiffusion at the coating-substrate interface and reducing the rapid diffusion paths for oxygen in the residual Cr coating during oxidation. Hence, MAO/Cr bilayer coating has excellent electrochemical corrosion resistance and high-temperature steam oxidation resistance which can be used to protect the Zr alloy claddings.

Declaration of competing interest

The authors declare that they have no known competing financial interests or personal relationships that could have appeared to influence the work reported in this paper.

CRediT authorship contribution statement

Zheng Wang: Writing – original draft, Investigation, Data curation. **Yingpeng Zhang:** Writing – review & editing, Writing – original draft. **Zhichao Han:** Visualization, Data curation. **Zhenyu Wang:** Validation, Supervision. **Wei Yang:** Software, Methodology.

Ming Li: Writing – review & editing, Supervision. **Aiyang Wang:** Writing – review & editing, Resources, Conceptualization. **Peiling Ke:** Writing – review & editing, Resources, Project administration, Formal analysis.

Acknowledgments

This work was financially supported by the [National Natural Science Foundation of China](#) (No. U22A20111), the Key Research and Development Program of Ningbo (No. 2023Z2DYF020062) and Leading Innovative and Entrepreneur Team Introduction Program of Zhejiang (No. 2024R01004).

Supplementary materials

Supplementary material associated with this article can be found, in the online version, at [doi:10.1016/j.jmst.2025.04.047](https://doi.org/10.1016/j.jmst.2025.04.047).

References

- [1] M. Daunys, R. Dundulis, A. Grybenas, P. Krasauskas, Nucl. Eng. Des. 238 (2008) 2536–2545.
- [2] A.S. Agazhanov, D.A. Samoshkin, S.V. Stankus, Thermophys. Aeromech. 28 (2021) 577–581.
- [3] V.E. Peletsky, High Temp.- High Press. 31 (1999) 627–632.
- [4] K.A. Terrani, J. Nucl. Mater. 501 (2018) 13–30.
- [5] J. Yang, M. Steinbrück, C. Tang, M. Große, J. Liu, J. Zhang, D. Yun, S. Wang, J. Alloys Compd. 895 (2022) 162450.
- [6] W. Zhang, Y. Qian, R. Sun, X. Lin, M. Yao, Y. Qiu, J. Yang, G. Cheng, J. Dong, Corros. Sci. 191 (2021) 109722.
- [7] Y. Wang, B. Chen, X.-Z. Wang, M. Chen, S. Li, G. Bai, J. Li, W. Gong, Corros. Sci. 217 (2023) 111099.
- [8] H.-G. Kim, I.-H. Kim, Y.-I. Jung, D.-J. Park, J.-Y. Park, Y.-H. Koo, J. Nucl. Mater. 465 (2015) 531–539.
- [9] J. Ko, J.W. Kim, H.W. Min, Y. Kim, Y.S. Yoon, J. Nucl. Mater. 561 (2022) 153562.
- [10] X.P. Wang, H.H. Guan, Y.Z. Liao, M.H. Zhu, C. Xu, X.Y. Jin, B. Liao, W.B. Xue, Y.W. Zhang, G.H. Bai, R.S. Wang, Corros. Sci. 187 (2021) 109494.
- [11] P. Lai, H. Zhang, L. Zhang, Q. Zeng, J. Lu, X. Guo, Wear 424 (2019) 53–61.
- [12] L. Zhang, P. Lai, Q. Liu, Q. Zeng, J. Lu, X. Guo, J. Nucl. Mater. 499 (2018) 401–409.
- [13] Y. Xiang, S. Zhao, C. Liu, H. Yang, W. Zhang, H. Wang, R. Zhang, H. He, S. Liu, Corros. Sci. 212 (2023) 110923.
- [14] X. Han, C. Chen, Y. Tan, W. Feng, S. Peng, H. Zhang, Corros. Sci. 174 (2020) 108826.
- [15] J.-C. Brachet, E. Roesne, J. Ribis, T. Guilbert, S. Urvoy, G. Nony, C. Toffolon-Masclot, M. Le Saux, N. Chaabane, H. Palanchar, A. David, J. Bischoff, J. Augereau, E. Pouillier, Corros. Sci. 167 (2020) 108537.
- [16] N. Attarzadeh, C.V. Ramana, Coatings 11 (2021) 620.
- [17] X. Qi, B. Jiang, R. Song, Corros. Sci. 199 (2022) 110164.
- [18] C. Xu, M. Zhu, H. Guan, C. Gao, X. Jin, J. Du, W. Xue, Corros. Sci. 209 (2022) 110711.
- [19] K.J. Wei, X.P. Wang, M.H. Zhu, H.H. Guan, C. Xu, W.B. Xue, J.L. Zhang, Corros. Sci. 181 (2021) 109216.
- [20] X.P. Wang, K.J. Wei, H.H. Guan, C. Xu, W.B. Xue, Y.W. Zhang, R.S. Wang, Surf. Coat. Technol. 407 (2021) 126768.
- [21] R. Lan, L. Dong, C. Wang, T. Liang, J. Tian, Rare Metal Mater. Eng. 42 (2013) 681–684.
- [22] R. Polini, M. Barletta, Diamond Relat. Mater. 17 (2008) 325–335.
- [23] C. Tang, M. Steinbrueck, M. Stueber, M. Grosse, X. Yu, S. Ulrich, H.J. Seifert, Corros. Sci. 135 (2018) 87–98.
- [24] Z. Wang, Z. Wang, A. Wang, W. Yang, P. Ke, Acta Metall. Sin. 60 (2024) 691–698.
- [25] Z. Wang, W. Li, Z. Wang, M. Li, A. Wang, P. Ke, Ceram. Int. 49 (2023) 22736–22744.
- [26] X.P. Wang, Y.Z. Liao, C. Xu, H.H. Guan, M.H. Zhu, C.L. Gao, X.Y. Jin, P. Pang, J.C. Du, B. Liao, W.B. Xue, J. Alloys Compd. 883 (2021) 160798.
- [27] W.T. Li, Z.Y. Wang, J.T. Shuai, B.B. Xu, A.Y. Wang, P.L. Ke, Ceram. Int. 45 (2019) 13912–13922.
- [28] X. Zuo, P. Ke, R. Chen, X. Li, M. Oden, A. Wang, Phys. Plasmas 24 (2017) 083507.
- [29] A. Anders, Surf. Coat. Technol. 257 (2014) 308–325.
- [30] S. Song, B. Chen, H. Li, R. Shi, C. Liu, B. Yang, G.F. de la Fuente, J. Mater. Sci. 58 (2023) 7136–7148.
- [31] C. Gautier, J. Machet, Thin Solid Films 289 (1996) 34–38.
- [32] Y. Meng, S. Zeng, Z. Teng, X. Han, H. Zhang, Thin Solid Films 730 (2021) 138699.
- [33] J.M. Zhang, K.W. Xu, M.R. Zhang, Acta Phys. Sin. 52 (2003) 1207–1212.
- [34] Y. Zhang, Q. Wang, G. Chen, C.S. Ramachandran, Surf. Coat. Technol. 403 (2020) 126380.
- [35] Y. Zhang, H. Li, L. Cui, W. Yang, G. Ma, R. Chen, P. Guo, P. Ke, A. Wang, Corros. Sci. 227 (2024) 111738.
- [36] Y. Zhang, X. Zhou, R. Chen, W. Yang, P. Guo, K. Nishimura, X. Li, A. Wang, Corros. Sci. 240 (2024) 112504.
- [37] Y. Li, H. Cao, H. Li, J. Yang, F. Qi, L. Lu, N. Zhao, Y. Zhou, X. Ouyang, Surf. Coat. Technol. 448 (2022) 128942.
- [38] X. Nie, Y. Tang, F. Zhao, S. Luo, W. He, C. Wei, J. Song, Z. Pang, ALP Adv. 12 (2022) 015211.
- [39] H.H. Kim, J.H. Kim, J.Y. Moon, H.S. Lee, J.J. Kim, Y.S. Chai, J. Mater. Sci. Technol. 26 (2010) 827–832.
- [40] H. Yeom, B. Maier, G. Johnson, T. Dabney, M. Lenling, K. Sridharan, J. Nucl. Mater. 526 (2019) 151737.
- [41] Z. Wang, Y. Zhang, S. Zhou, Z. Wang, Y. Yao, A. Wang, M. Li, P. Ke, Corros. Commun. 14 (2024) 49–57.
- [42] Z. Han, Z. Wang, Z. Wang, S. Tan, A. Wang, Z. Piao, P. Ke, Surf. Coat. Technol. 488 (2024) 130941.
- [43] X. Wang, J.A. van Bokhoven, D. Palagin, Phys. Chem. Chem. Phys. 19 (2017) 30513–30519.